Check for updates

In Situ "Chainmail Catalyst" Assembly in Low-Tortuosity, Hierarchical Carbon Frameworks for Efficient and Stable Hydrogen Generation

Yiju Li, Tingting Gao, Yonggang Yao, Zhenyu Liu, Yudi Kuang, Chaoji Chen, Jianwei Song, Shaomao Xu, Emily M. Hitz, Boyang Liu, Rohit J. Jacob, Michael R. Zachariah, Guofeng Wang, and Liangbing Hu*

The chainmail catalysts (transition metals or metal alloys encapsulated in carbon) are regarded as stable and efficient electrocatalysts for hydrogen generation. However, the fabrication of chainmail catalysts usually involves complex chemical vapor deposition (CVD) or prolonged calcination in a furnace, and the slurry-based electrode assembly of the chainmail catalysts often suffers from inferior mass transfer and an underutilized active surface. In this work, a freestanding wood-based open carbon framework is designed embedded with nitrogen (N) doped, few-graphene-layer-encapsulated nickel iron (NiFe) alloy nanoparticles (N-C-NiFe). 3D wood-derived carbon framework with numerous open and low-tortuosity lumens, which are decorated with carbon nanotubes (CNTs) "villi", can facilitate electrolyte permeation and hydrogen gas removal. The chainmail catalysts of the N-C-NiFe are uniformly in situ assembled on the CNT "villi" using a rapid heat shock treatment. The high heating and quenching rates of the heat shock method lead to formation of the well-dispersed ultrafine nanoparticles. The self-supported wood-based carbon framework decorated with the chainmail catalyst displays high electrocatalytic activity and superior cycling durability for hydrogen evolution. The unique heat shock method offers a promising strategy to rapidly synthesize well-dispersed binary and polynary metallic nanoparticles in porous matrices for high-efficiency electrochemical energy storage and conversion.

1. Introduction

Water electrolysis is regarded as the facile, efficient, and sustainable technology for mass production of high-purity molecular hydrogen.[1–7] Among the electrocatalysts for hydrogen evolution reaction (HER), Pt and Pt-based alloys show the best electrochemical performance with small Tafel slope and overpotential.[8–12] Unfortunately, the commercial applications of the Pt group electrocatalysts are greatly hindered by their high cost and scarcity. Exploring the cost-effective, stable, and high-performance alternatives to noble metal electrocatalysts is critically necessary to enable sustainable hydrogen economy. Moreover, constructing self-supported open and porous electrode structures without using binders can simplify the tedious slurry-based electrode assembly process and enhance the mass transfer, which is promising for large-scale practical application. Toward this end, low-cost and stable core–shell chainmail catalysts have been developed recently toward efficient HER.[13–18] These chainmail catalysts operate on the principle of allowing an electron from the core of transition metal or metal alloy to penetrate through the carbon shell to enhance the catalytic reactivity.[19] At the same time, the carbon shell can protect the core of nanoparticles from deterioration in harsh conditions, such as strong acidic electrolyte and oxygen-rich atmosphere. Nevertheless, nearly all reported works about the preparation of chainmail catalysts involve a prolonged high-temperature calcination and cooling stage in the furnace, and some even need complex and expensive CVD methods or multistep synthesis processes.[19–22] The conventional pyrolysis in the furnace is usually achieved by radiative heating using a resistive filament, and the slow heating and cooling rates could possibly result in agglomeration and degradation of metal nanoparticles.[23] Therefore, it is significant to develop a fast-responding and controllable high-temperature treatment method for the assembly of chainmail catalysts in freestanding porous carbon frameworks over a short time to avoid or mitigate agglomeration.

Dr. Y. Li, T. Gao, Dr. Y. Yao, Y. Kuang, Dr. C. Chen, Dr. J. Song,
Dr. S. Xu, E. M. Hitz, B. Liu, Prof. L. Hu
Department of Materials Science and Engineering
University of Maryland
College Park, MD 20742, USA
E-mail: binghu@umd.edu
Z. Liu, Prof. G. Wang
Department of Mechanical Engineering and Materials Science
University of Pittsburgh
PA 15261, USA
R. J. Jacob, Prof. M. R. Zachariah
Department of Chemical Engineering and Chemistry
University of Maryland
College Park, MD 20742, USA

In our work, the rapid in situ self-assembly of the core-shell N-C-NiFe nanoparticles in the porous carbonized wood (CW) based framework was first achieved using the heat shock treatment method through ultrafast Joule heating. Owing to the ultrahigh heating and quenching rates, the metal salt precursors decompose and then redistribute rapidly on the carbon support to nucleate into ultrafine metal alloy nanoparticles. The thermal shock induced N-C-NiFe nanoparticles possess a smaller average size of 22.5 nm and thinner graphene shells (one to four layers) than the NiFe nanoparticles treated with conventional calcination in the furnace (average size: 175 nm; graphene shells: nine layers). The N-C-NiFe electrocatalysts uniformly anchor on the CNTs, which grow in situ inside the wood-derived carbon microchannels (CW-CNT@N-C-NiFe), contributing to fast electron transport. The open and low-tortuosity microchannels of the CW-CNT framework can facilitate unimpeded hydrogen gas release and electrolyte permeation. As a result, the CW-CNT@N-C-NiFe electrode exhibited impressive electrochemical performance toward hydrogen evolution with a small Tafel slope of 52.8 mV dec^{-1} and an overpotential of 179 mV at 10 mA cm^{-2} with favorable long-term cycling stability. The newly developed facile yet effective heat shock treatment method is a potential alternative for rapid in situ self-assembly of nanoparticles in conductive supports for high-efficiency electrocatalysis.

2. Results and Discussion

The preparation process of the CW-CNT@N-C-NiFe electrode is briefly demonstrated in **Figure 1**a. The natural wood was cut perpendicular to its growth direction and carbonized to obtain the porous and aligned carbon framework. The CNT arrays were then grown inside the microchannels through facile in situ pyrolysis deposition to increase the active sites for immobilization of catalysts. After dipping the CW-CNT sample into the precursor solutions containing Ni and Fe salts and drying, the N-C-NiFe electrocatalysts were rapidly self-assembled in the CW-CNT framework using the ultrafast heat pulse treatment. Owing to the open and low-tortuosity wood structure, the electrolyte can easily permeate into the porous framework of the CW-CNT@N-C-NiFe during the HER process, and the generated hydrogen gas on the catalysts' surface is able to unimpededly release from the microchannels without blocking the pathway of mass transfer (Figure 1b). Additionally, the core–shell N-C-NiFe nanoparticles are uniformly anchored on the CNTs, which contribute to the formation of electron "highways" for fast charge transfer on the surface of N-C-NiFe (Figure 1c).

Figure 2a shows the schematic representation of the device for conducting an ultrafast heat shock treatment. The sample was mounted on a homemade glass shelf and then put into a sealed vacuum chamber. A direct current pulse controlled by a programmed Keithley power source is passed through the sample to generate heat (Figure 2b). The induced high temperature can be controlled by the resistance of sample and direct current pulse.[24] The details of time and temperature measurement are shown in Method S1 and Figure S1 in the Supporting Information. Figure 2c displays the output spectra versus time, which are collected from 30 channels spanning from 440 to 858 nm. The intensity of each channel reaches the highest value when the time is about 45 milliseconds (ms).
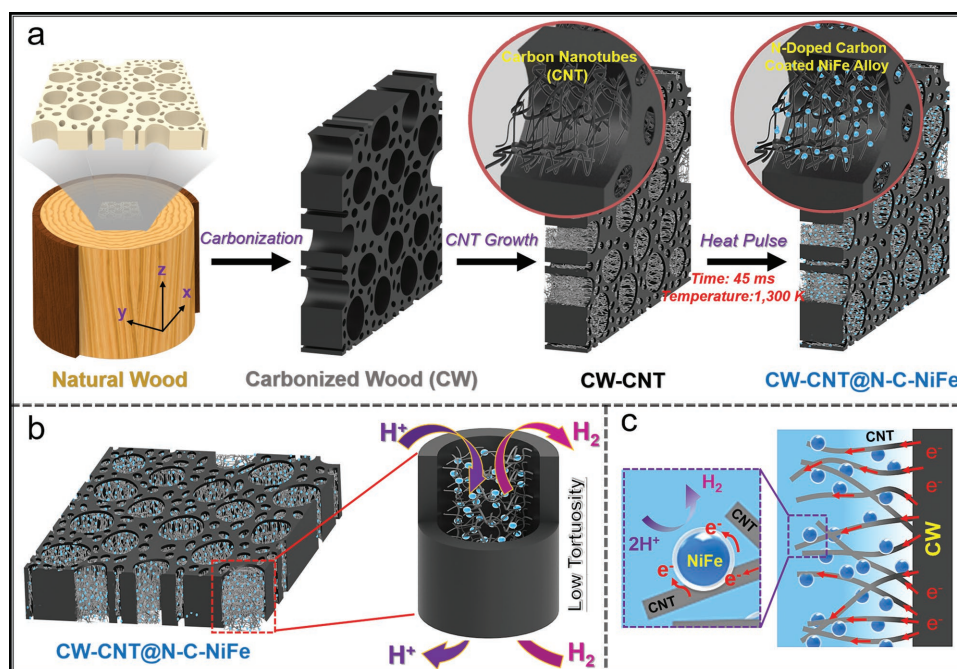
Figure 1. Schematic illustration of the preparation process and mechanism. a) Schematic representation showing the fabrication process of the CW-CNT@N-C-NiFe electrode. The core–shell N-C-NiFe nanoparticles were synthesized using rapid heat shock treatment (temperature: ≈1300 K; heating time: 45 ms). b) Schematic illustration showing the open and low-tortuosity structure of the CW-CNT@N-C-NiFe electrode. c) Schematic illustration of the hydrogen evolution reaction on the N-C-NiFe nanoparticles. Electrons travel along the CNT to the N-C-NiFe nanoparticles for the reduction of protons.
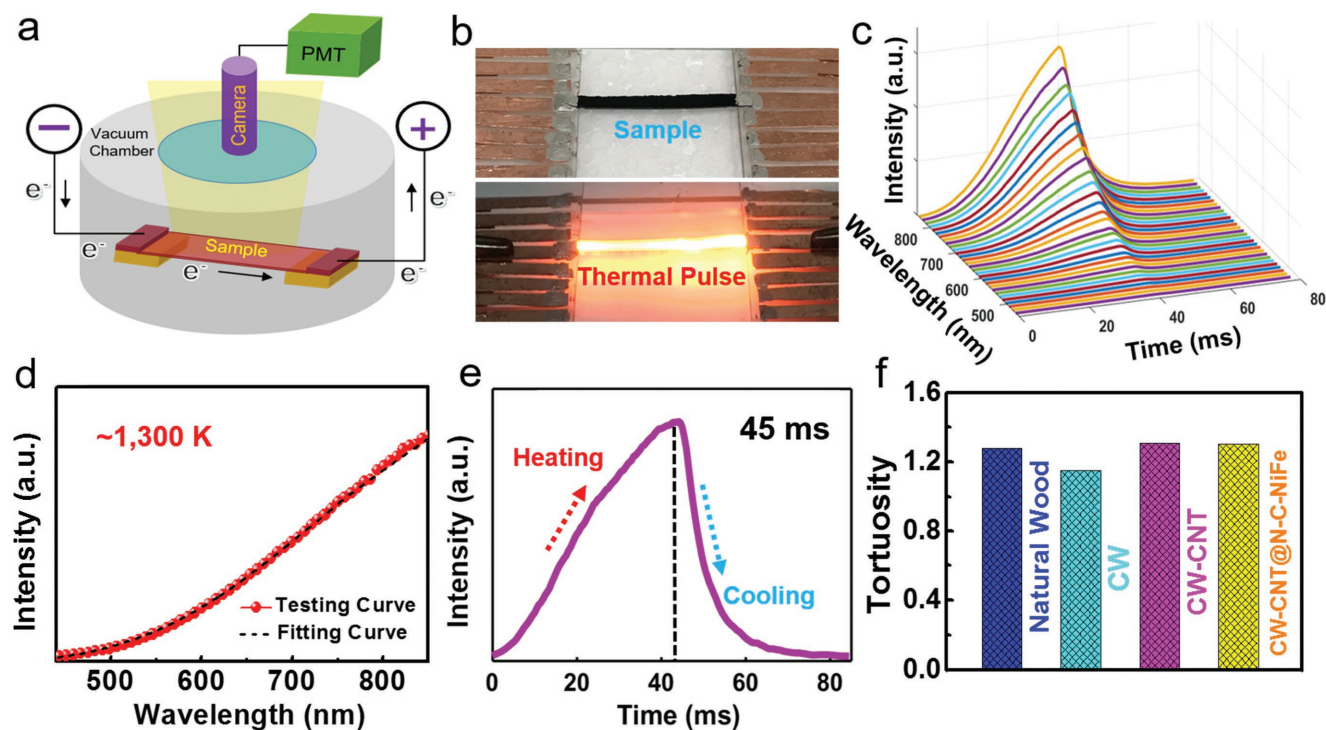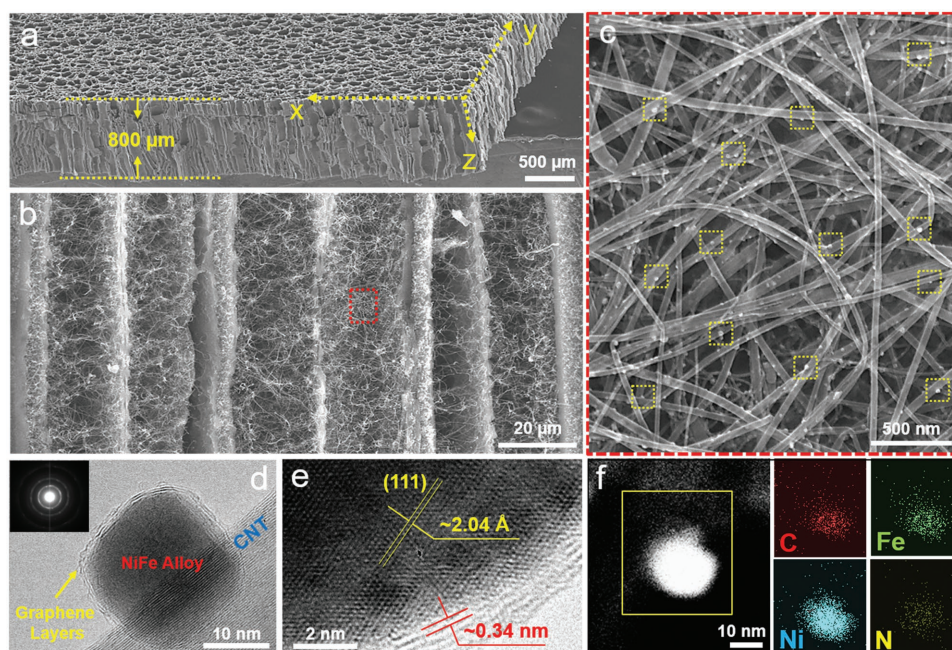
Figure 2. Temperature and time measurement of the ultrafast thermal pulse method. a) Schematic representation showing the setup of conducting thermal pulse treatment in a vacuum chamber. b) Photo images showing the sample before and during the heat shock treatment. The sample was mounted on a glass shelf. c) High-speed spectroscopic curves during the thermal pulse process with intensities collected over 30 channels (440–858 nm). d) Irradiance spectrum at the maximum intensity for each channel during the heat pulse treatment. The blackbody radiation model was used to fit the spectrum. e) Intensity curve versus time showing the ultrafast heating and cooling process. The curve is extracted from the spectrum on the 858 nm channel. f) Comparison of tortuosity values of the various wood-based samples. The tortuosity values of the natural wood, CW, CW-CNT, and CW-CNT@N-C-NiFe are 1.28, 1.15, 1.31, and 1.30, respectively.

The irradiance spectrum at the maximum intensity for each channel was fitted to blackbody radiation equation to extract the maximum temperature (≈1300 K) (Figure 2d). The time duration is confirmed by the time-resolved spectrum extracted from the 858 nm channel (Figure 2e). The temperature can reach its peak within only tens of milliseconds and decrease rapidly. As the slow heating and cooling rates can cause particle agglomerations and coalescence, the ultrafast heat shock in our report minimizes the particle coarsening and leads to uniform dispersion of nanoparticles throughout the CW-CNT sample.

Low tortuosity of the electrode is critical for quick mass transfer during the hydrogen generation reaction. We compared the tortuosity of the CW-CNT@N-C-NiFe electrode treated with heat shock with other samples (Figure 2f). The tortuosity was tested using the alternating current (AC) impedance measurement (Method S2 and Figure S2, Supporting Information). The tortuosity values of the natural wood, CW, CW-CNT, and CW-CNT@N-C-NiFe were calculated to be 1.28, 1.15, 1.31, and 1.30, respectively. We observed the bare CW to have a lower tortuosity value compared to the CW-CNT and CW-CNT@N-C-NiFe electrodes, which we attribute to the filling of CNT and electrocatalysts inside the microchannels. Notably, even for the CW-CNT@N-C-NiFe electrode, its tortuosity is much lower than those of the slurry-coated electrodes (3–30),[25] expediting electrolyte permeation and release of hydrogen bubbles.

The morphology of the CW-CNT@N-C-NiFe composite was investigated using the scanning electron microscopy (SEM). Wood has naturally porous and low-tortuosity microstructures along its growth direction (Figure S3, Supporting Information). After carbonization, the elongated and aligned microchannels of the wood can be perfectly reserved (Figure S4, Supporting Information). **Figure 3**a displays the side view of the CW slice with a typical thickness of 800 µm. The CNT was grown in situ on the inner walls of the microchannels to form interconnected conductive networks. The CNT growth process can be facilely controlled by adjusting the time duration (Figure S5, Supporting Information). Figure S6 in the Supporting Information shows the top surface of the CW-CNT composite with a growth time of 120 min. The microchannels are full of the interconnected CNTs with good crystallinity (Figure S7, Supporting Information). Figure 3b displays the cross-section of the CW-CNT@N-C-NiFe composite. It can be confirmed that the CNT is not only dispersed near the surface but also uniformly distributed throughout the microchannels. The enlarged SEM image reveals numerous nanoparticles are homogenously loaded on the CNT (Figure 3c). The energy-dispersive spectra of the CW-CNT@N-C-NiFe composite confirm the uniform dispersion of the N-C-NiFe nanoparticles in the CW-CNT framework (Figure S8, Supporting Information). From the particle size analysis, it can be observed that the N-C-NiFe nanoparticles have a concentrated size distribution and the average

**ADVANCED
SCIENCE NEWS**

www.advancedsciencenews.com

**ADVANCED
ENERGY
MATERIALS**

www.advenergymat.de

Figure 3. Morphology characterizations of the CW-based samples. a) SEM image showing the side view of the CW slice. The typical thickness of the CW is about 800 µm. b) SEM image showing the cross-section of the CW-CNT@N-C-NiFe composite. The aligned and low-tortuosity microchannels are filled with CNT. c) SEM image showing the uniform dispersion of the N-C-NiFe nanoparticles. d) TEM image of a single N-C-NiFe nanoparticle, which anchors on the CNT. The NiFe alloy nanoparticle is encapsulated by the few graphene layers. Inset in panel (d) is the SAED patterns of the N-C-NiFe nanoparticles. e) HRTEM image of the N-C-NiFe nanoparticle. The nanoparticle has a lattice spacing of about 2.04 Å, corresponding to the (111) crystalline plane of the NiFe alloy. The distance between neighboring graphene layers is about 0.34 nm. f) HAADF-STEM image of the N-C-NiFe nanoparticle and the corresponding EDX elemental maps (C, Fe, Ni, and N).
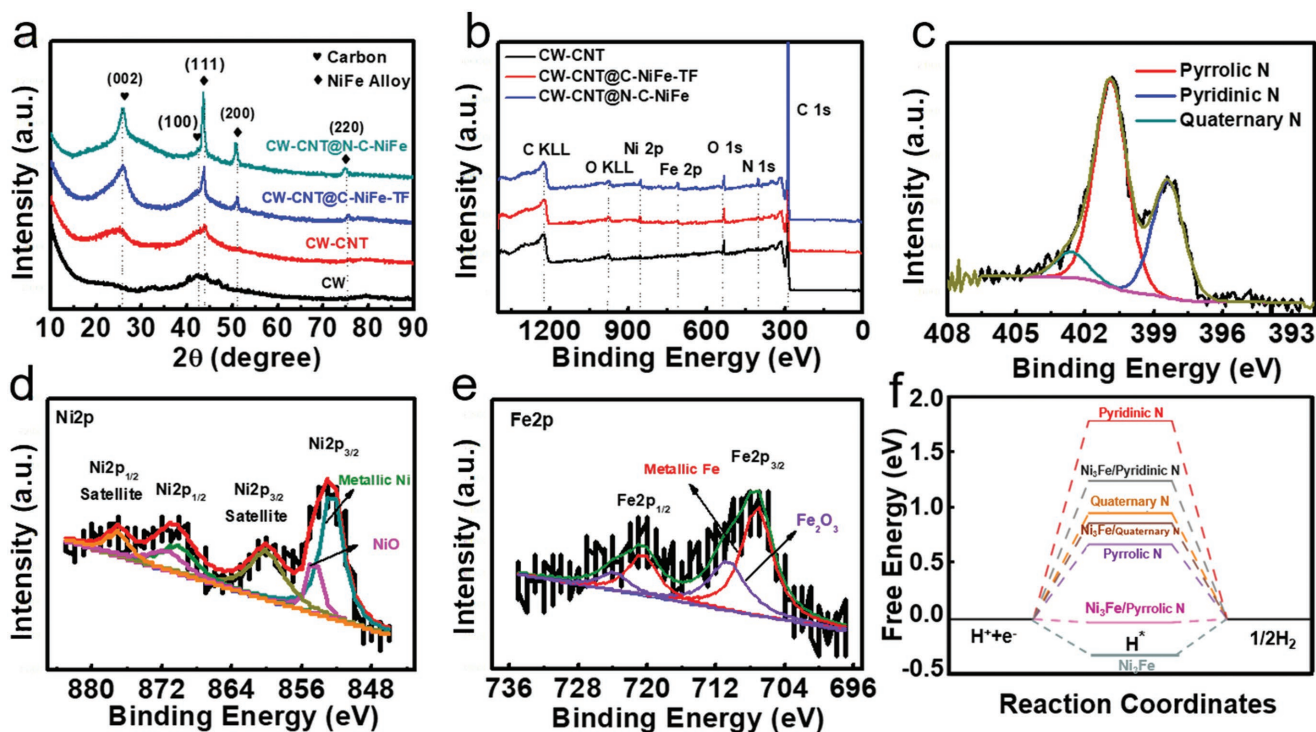
size is about 22.5 nm (Figure S9a, Supporting Information). As a comparison, the NiFe alloy nanoparticles treated with conventional pyrolysis in a tube furnace (TF) have a scattered size distribution and the maximum diameter can reach up to ≈500 nm, which is 22.2 times larger than that of the heat shock triggered N-C-NiFe nanoparticles (Figure S10a,b, Supporting Information).

Figure 3d shows the transmission electron microscopy (TEM) image of the single N-C-NiFe nanoparticle on a CNT. The NiFe alloy nanoparticles are encapsulated by few graphene layers (one to four layers) (Figure S9b–e, Supporting Information). However, the NiFe nanoparticles calcined in the tube furnace (denoted as C-NiFe-TF) have a thicker graphene shell (nine layers) than the N-C-NiFe nanoparticles (Figure S10c,d, Supporting Information). The well-defined selected area electron diffraction (SAED) patterns manifest the polycrystalline nature of the N-C-NiFe nanoparticles (Inset in Figure 3d).[26] The high-resolution TEM (HRTEM) image further confirms the NiFe nanoparticle is coated by the graphene shells with a layer distance of ≈0.34 nm (Figure 3e).

The spacing of the two lattice fringes on the nanoparticles is about 0.204 nm, corresponding to the (111) plane of the NiFe alloy.[27] The high angle annular dark field scanning transmission electron microscopy (HAADF-STEM) image of the N-C-NiFe nanoparticle and the corresponding energy-dispersive X-ray (EDX) elemental maps are shown in Figure 3f. The results indicate that the N heteroatoms are uniformly doped on the graphene layers. The probe-corrected scanning transmission electron microscopy-electron energy-loss spectroscopy

(STEM-EELS) line scan analysis was further conducted to investigate the Ni and Fe atoms distribution on the near-surface on the nanoparticles (Figure S11, Supporting Information).[28,29] The N-C-NiFe nanoparticle demonstrates nearly symmetrical Ni and Fe EELS profiles, which manifests the homogenous dispersion of Ni and Fe atoms. Moreover, the normalized intensity of the Ni element is almost three times larger than that of Fe element, meaning the atomic ratio of Ni to Fe is about 3:1. The atomic ratio of Ni to Fe is further verified by the results of inductively coupled plasma mass spectrometry (ICP-MS) (Ni:Fe = 3.1:1).

The phase structure of the samples was investigated using the X-ray diffraction (XRD) (**Figure 4**a). The diffraction peaks located at ≈25° and ≈43° are assigned to the (002) and (100) crystal planes of carbon, respectively.[30] For the samples of CW-CNT@C-NiFe-TF and CW-CNT@N-C-NiFe, the diffraction peaks at 44.3°, 51.5°, and 75.9° correspond to the (111), (200), and (220) crystal planes of the Ni$_3$Fe alloy (Awaruite, JCPDS Card No. 38–0419), respectively. We further explored the chemical composition information of N, Fe, and Ni species on the surface by the X-ray photoelectron spectroscopy (XPS). Figure 4b shows the wide-scan XPS spectra of the samples. The elements of C, N, Fe, and Ni can be clearly observed in the sample of CW-CNT@N-C-NiFe, agreeing with the observation from the EDX elemental maps. According to the results of XPS, we can observe that the atomic content of N for the CW-CNT@N-C-NiFe electrode is about 3.02 at% (excluding Ni and Fe) (Table S1, Supporting Information). Figure 4c displays the high-resolution of the N1s peak, which can be deconvoluted

ADVANCED
SCIENCE NEWS
www.advancedsciencenews.com

ADVANCED
ENERGY
MATERIALS
www.advenergymat.de

Figure 4. Structure and composition characterizations of the carbon samples. a) XRD patterns of the CW, CW-CNT, CW-CNT@C-NiFe-TF, and CW-CNT@N-C-NiFe. b) Wide-scan XPS spectra of the CW-CNT, CW-CNT@C-NiFe-TF, and CW-CNT@N-C-NiFe. c) High-resolution XPS spectrum of the N1s peak. The N1s spectrum can be deconvoluted into pyrrolic N, pyridinic N, and quaternary N, respectively. d) High-resolution XPS spectrum of the Ni2p peak. e) High-resolution XPS spectrum of Fe2p peak. f) Calculated ΔG_{H*} diagram of various models (pyrrolic/pyridinic/quaternary N doped graphene with and without encapsulated Ni_3Fe clusters).

into quaternary N (402.6 eV), pyridinic N (398.3 eV), and pyrrolic N (400.8 eV).[31] The pyrrolic N is the dominant N-containing functional group among the three types of N. The high-resolution XPS spectra of Ni2p and Fe2p are shown in Figure 4d,e, respectively. The peak intensity of Ni2p and Fe2p is relatively weak, as they are encapsulated in the graphene layers.[32] The Ni2p and Fe2p spectra reveal that the Ni and Fe mainly exist in the metallic form.[33]

Free energy of hydrogen adsorption (ΔG_{H*}) is an important indicator in the theoretical prediction of the electroactivity of electrode materials toward HER.[34] If the ΔG_{H*} is very negative, the hydrogen atom can be strongly absorbed on the electrode surface, resulting in the sluggish Tafel or Heyrovsky step. If the ΔG_{H*} is quite positive, the hydrogen atom can be hardly absorbed on the electrode surface, which will lead to slow Volmer step and then limit the overall reaction rate. Therefore, an ideal electrocatalyst for hydrogen generation should possess moderate ΔG_{H*} (ΔG_{H*} close to zero). To investigate the ΔG_{H*} of the N-C-NiFe nanoparticles, we carried out the density functional theory (DFT) calculations using the Vienna Ab-initio Simulation Package (VASP) within the formulism of plane wave basis and projector augmented wave method. The details of the calculation are shown in the Method S3 in the Supporting Information. To simplify the computational process, we adopted the Ni_3Fe cluster as the model to conduct the calculation based on the results of ICP-MS and STEM-EELS. Three types of N were embedded in the graphene matrix: quaternary N, pyridinic N, and pyrrolic N. In all three cases, the Ni_3Fe cluster was placed

on the one side of graphene layer and at a position near the N dopant. The hydrogen atom was adsorbed on the other side of graphene layer and near the stable carbon site adjacent to the N dopant (Figure S12, Supporting Information). The free energy of the adsorbed state was calculated as followed:

$$\Delta G_{H*} = \Delta E_H + \Delta E_{ZPE} - T\Delta S_H \tag{1}$$

Where ΔE_H is the hydrogen chemisorption energy, ΔE_{ZPE} is the zero-point energy correction of H and $T\Delta S_H$ is the entropic correction between the adsorbed state and gas phase. In this work, ΔS_H was taken from the reported literature.[35]

The calculated free energy diagram for HER is shown in Figure 4f. Our result shows that the ΔG_{H*} is greater than zero for all optimized structures other than Ni_3Fe/pyrrolic N-doped graphene, indicating an endothermic process for proton transfer, whereas on Ni_3Fe/pyrrolic N-doped graphene, the process is exothermic. Among the three types of N-doped graphene structures, the pyrrolic N-doped graphene possesses a lowest ΔG_{H*} of 0.67 eV. This prediction is consistent with the result reported by Yang et al. about the first principles calculation on N-doped graphene layers using Perdew–Becke–Ernzerhof functionals.[20] The ΔG_{H*} of the Ni_3Fe cluster without covered by N-doped graphene is −0.35 eV, indicating the relative strong adsorption of H atoms on the surface of the Ni_3Fe cluster. For the N-doped graphene layer wrapped Ni_3Fe cluster, a decrease in the ΔG_{H*} is found as compared with the corresponding structure without Ni_3Fe cluster, which

**ADVANCED
SCIENCE NEWS**
www.advancedsciencenews.com

**ADVANCED
ENERGY
MATERIALS**
www.advenergymat.de

indicates the Ni$_3$Fe cluster is beneficial for the improvement of electrocatalytic activity through the optimization of H atom adsorption. Among all cases investigated, the optimized pyrrolic N-doped graphene wrapped Ni$_3$Fe cluster has a ΔG_{H*} of –0.03 eV, which is predicted to have the best electrocatalytic performance for HER. The calculated results of ΔG_{H*} for all structures were summarized in Table S2 in the Supporting Information. Our further analysis on the charge density and electronic structure in Figure S13a in the Supporting Information reveals that some electron charge will transfer from the Ni$_3$Fe cluster to the N-doped graphene. This charge transfer could lead to a decrease in local work function and increase in the density of states near the fermi level (Figure S13b, Supporting Information) and therefore an enhanced hydrogen binding.[36] This synergistic effect between the encapsulated metallic cluster and the N-doped graphene is consistent with the concept of chainmail HER catalysts.

Before testing the hydrogen generation performance, we have evaluated the wettability of the CW-CNT@N-C-NiFe electrode. Favorable wettability is beneficial for the contact between the electrolyte and electrode, contributing to the full use of the active surface of electrode materials. As shown in Figure S14 in the Supporting Information, the electrolyte droplet can be completely absorbed into the porous electrode within a short time of 0.5 s, which indicates the excellent electrolyte wettability of the electrode. The linear sweep voltammetry polarization curves

of the samples are displayed in **Figure 5a**. The commercial 40 wt% Pt/C composite electrode was also tested for comparison. The pure CW shows the worst HER activity of the varieties tested. The electrocatalytic activity of CW-CNT is slightly improved owing to the increased contact area of the electrode, but is still poor for hydrogen generation. The electrochemical double-layer capacitance (C_{dl}) between the electrode and electrolyte can be used to estimate the effective surface area of the solid-liquid interface by cyclic voltammetry (CV). We measured the C_{dl} of the CW-CNT and CW frameworks by integrating the area of their CV curves to compare their specific surface areas. The C_{dl} of CW-CNT and CW is 50.4 and 18.1 mF cm^{-2}, respectively (Figure S15, Supporting Information), confirming the increased specific surface area after the growth of CNT in the CW framework. As expected, the commercial 40 wt% Pt/C composite electrode has the best HER performance with a low overpotential of 59 mV at a current density of 10 mA cm^{-2}. For the CW-CNT@N-C-NiFe electrode, it exhibited enhanced electroactivity for HER with an overpotential of 179 mV at a current density of 10 mA cm^{-2} when compared with the CW-CNT@C-NiFe-TF electrode (226 mV at 10 mA cm^{-2}). We compared the performance of our electrode materials with the previously reported works involving nonprecious metals for HER and summarized the results in Table S3 in the Supporting Information. The performance of our heat shock triggered CW-CNT@N-C-NiFe is one of the best among the various chainmail catalysts.
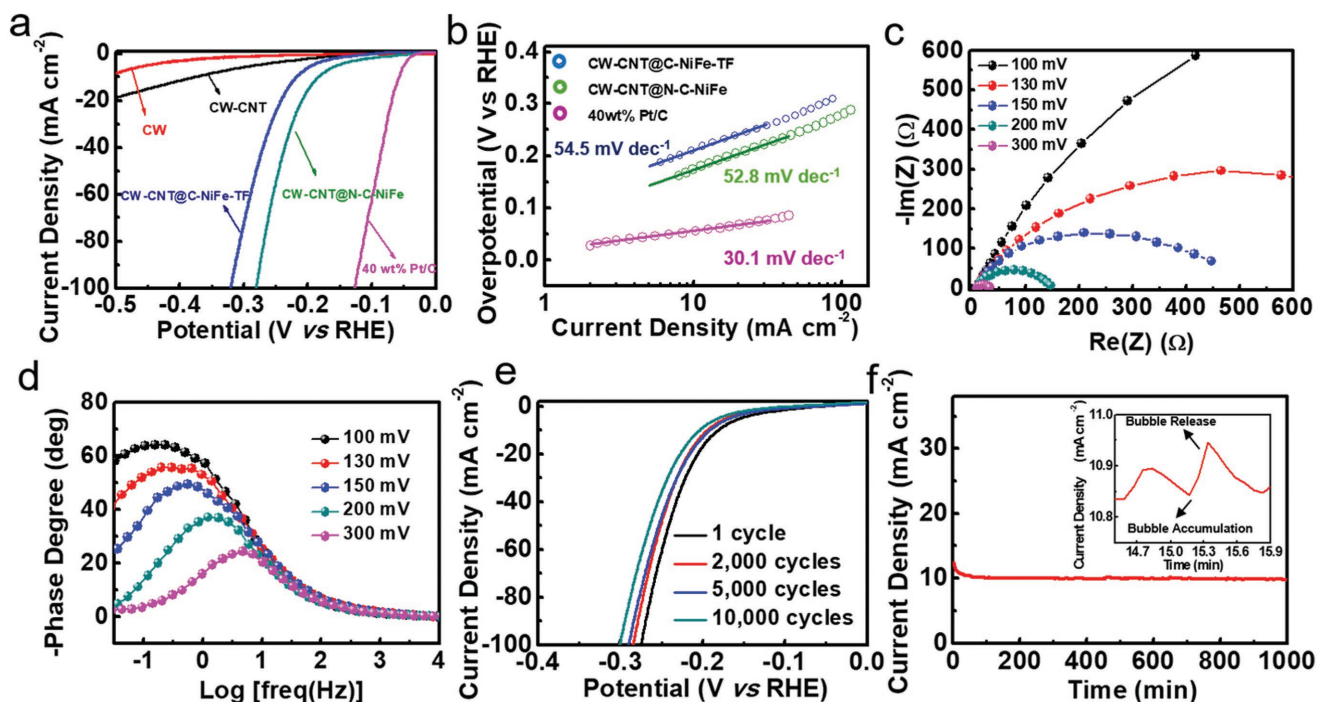
Figure 5. Electrochemical performance of the as-prepared electrodes in 0.5 M H$_2$SO$_4$. a) Polarization curves of the CW, CW-CNT, CW-CNT@C-NiFe-NF, commercial 40 wt% Pt/C, and CW-CNT@N-C-NiFe electrodes. b) Tafel plots of the CW-CNT@C-NiFe-NF, commercial 40 wt% Pt/C, and CW-CNT@N-C-NiFe electrodes. c) Nyquist plots of the CW-CNT@N-C-NiFe electrode at various overpotentials (vs RHE). The charge transfer resistance decreases significantly with increasing overpotentials, suggesting faster HER kinetics at the solid/liquid interface at higher overpotential. d) Bode phase plots of the CW-CNT@N-C-NiFe electrode at various overpotentials. e) Polarization curves of the CW-CNT@N-C-NiFe electrode after 1, 2000, 5000, and 10 000 cycles. The polarization curve of the CW-CNT@N-C-NiFe electrode after 10 000 cycles is similar to the initial cycle, indicating superior cycling performance. f) The time-dependent current density of the CW-CNT@N-C-NiFe electrode at an overpotential of 185 mV for 1000 min. Inset showing the fluctuation of the current density caused by the accumulation and release of hydrogen bubbles.

**ADVANCED
SCIENCE NEWS**

www.advancedsciencenews.com

**ADVANCED
ENERGY
MATERIALS**

www.advenergymat.de

To investigate the potential mechanisms of HER on the catalysts, we generated Tafel curves using the various electrodes (Figure 5b). The Tafel slope extracted from the linear region indicates the rate-limiting step of the HER.[37] The Tafel slopes of the 40 wt% Pt/C, CW-CNT@C-NiFe-TF, and CW-CNT@N-C-NiFe electrode are 30.1, 54.5, and 52.8 mV dec^{-1}, respectively. For the 40 wt% Pt/C electrode, the Tafel reaction may be the rate-limiting step (H*+H*→H$_2$). The Tafel slope of the CW-CNT@N-C-NiFe indicates that the HER process probably occurs through a Volmer–Heyrovsky mechanism.[38] The rapid discharge step (Volmer reaction: H$^+$+e$^-$→H*) occurs first and is directly followed by the electrochemical desorption (Heyrovsky reaction: H*+H$^+$+e$^-$→H$_2$), which we identify as the possible rate-limiting step.

Electrochemical impedance spectroscopy was utilized to further explore the kinetics of hydrogen generation on the CW-CNT@N-C-NiFe electrode. Figure 5c shows the Nyquist plots of the CW-CNT@N-C-NiFe electrode under different overpotentials versus reversible hydrogen electrode (RHE). The presence of one semicircle suggests there is only one time constant to characterize the equivalent circuit of HER, in which a resistor and a capacitor are in parallel.[39] The diameter of the semicircle represents the charge transfer resistance (R_{ct}) during the process of HER at the solid/liquid interface.[40] With the increase in overpotential, the R_{ct} decreases, suggesting faster HER kinetics. Additionally, the lack of Warburg resistance at the low-frequency region suggests the charge transfer at the interface is rapid and the HER is kinetically controlled. Figure 5d shows the Bode phase plots of CW-CNT@N-C-NiFe electrode. The dependence of the phase angle on the frequency indicates there is an extra resistor element in the equivalent circuit connected in series with the aforementioned two components.[39]

Accelerated cycling measurements were conducted to evaluate the durability of the electrode (Figure 5e). The CW-CNT@N-C-NiFe electrode shows similar performance to the initial measurement with favorable cycling stability even after 10000 cycles. The chronoamperometry measurement was further conducted to investigate the long-term stability under a designated overpotential (Figure 5f). The current retains stable for 480 min under an overpotential of 185 mV without observable degradation, which confirms the superior cycling durability. The fluctuation of current density in the inset in Figure 5f may be attributed to the generation and release of hydrogen bubbles.

3. Conclusions

In summary, the rapid self-assembly of chainmail catalyst nanoparticles (N-C-NiFe) in the open and low-tortuosity CW-CNT framework was first achieved using the heat shock treatment method. The ultrahigh heating and quenching rates during the heat shock process can effectively confine the migration and prevent the coalescence of NiFe nanoparticles, resulting in well-dispersed ultrafine nanoparticles. The porous CW-CNT framework with numerous aligned microchannels can facilitate electrolyte permeation and hydrogen bubble release. As a result, the freestanding CW-CNT@N-C-NiFe electrode shows high electrocatalytic activity and durability toward hydrogen

generation. The free energy of hydrogen adsorption on the optimized N-C-NiFe electrocatalyst is a mere −0.03 eV. The 3D porous CW-CNT@N-C-NiFe electrode possesses a low Tafel slope of 52.8 mV dec^{-1} and an overpotential of 179 mV at a current density of 10 mA cm^{-2}. Even after 10 000 cycles, the polarization curve of the CW-CNT@N-C-NiFe electrode remains largely unchanged. The rapid in situ self-assembly of ultrafine chainmail catalyst nanoparticles in self-supported porous carbon matrices using the facile yet effective thermal shock treatment could be a promising strategy for efficient and scalable hydrogen generation.

Supporting Information

Acknowledgements

Conflict of Interest

The authors declare no conflict of interest.

Keywords

[1] J. Feng, F. Lv, W. Zhang, P. Li, K. Wang, C. Yang, B. Wang, Y. Yang, J. Zhou, F. Lin, G.-C. Wang, S. Guo, *Adv. Mater.* **2017**, *29*, 1703798.

[2] H. J. Qiu, Y. Ito, W. Cong, Y. Tan, P. Liu, A. Hirata, T. Fujita, Z. Tang, M. Chen, *Angew. Chem., Int. Ed.* **2015**, *54*, 14031.

[3] Y. Liu, Q. Li, R. Si, G.-D. Li, W. Li, D.-P. Liu, D. Wang, L. Sun, Y. Zhang, X. Zou, *Adv. Mater.* **2017**, *29*, 1606200.

[4] W. Chen, J. Pei, C.-T. He, J. Wan, H. Ren, Y. Zhu, Y. Wang, J. Dong, S. Tian, W.-C. Cheong, S. Lu, L. Zheng, X. Zheng, W. Yan, Z. Zhuang, C. Chen, Q. Peng, D. Wang, Y. Li, *Angew. Chem.* **2017**, *129*, 1.

[5] D. Voiry, J. Yang, M. Chhowalla, *Adv. Mater.* **2016**, *28*, 6197.

ADVANCED
SCIENCE NEWS

www.advancedsciencenews.com

ADVANCED
ENERGY
MATERIALS

www.advenergymat.de

[6] M. S. Faber, S. Jin, *Energy Environ. Sci.* **2014**, *7*, 3519.

[7] X. Zou, Y. Zhang, *Chem. Soc. Rev.* **2015**, *44*, 5148.

[8] M. C. Tavares, S. A. S. Machado, L. H. Mazo, *Electrochim. Acta* **2001**, *46*, 4359.

[9] H. Zhou, F. Yu, Y. Liu, J. Sun, Z. Zhu, R. He, J. Bao, W. A. Goddard, S. Chen, Z. Ren, *Energy Environ. Sci.* **2017**, *10*, 1487.

[10] J. Wang, F. Xu, H. Jin, Y. Chen, Y. Wang, *Adv. Mater.* **2017**, *29*, 1605838.

[11] K. Xu, H. Ding, M. Zhang, M. Chen, Z. Hao, L. Zhang, C. Wu, Y. Xie, *Adv. Mater.* **2017**, *29*, 1606980.

[12] X. Cheng, Y. Li, L. Zheng, Y. Yan, Y. Zhang, G. Chen, S. Sun, J. Zhang, *Energy Environ. Sci.* **2017**, *10*, 2450.

[13] X. Dai, Z. Li, Y. Ma, M. Liu, K. Du, H. Su, H. Zhuo, L. Yu, H. Sun, X. Zhang, *ACS Appl. Mater. Interfaces* **2016**, *8*, 6439.

[14] L. Lang, Y. Shi, J. Wang, F.-B. Wang, X.-H. Xia, *ACS Appl. Mater. Interfaces* **2015**, *7*, 9098.

[15] D. Hou, W. Zhou, K. Zhou, Y. Zhou, J. Zhong, L. Yang, J. Lu, G. Li, S. Chen, *J. Mater. Chem. A* **2015**, *3*, 15962.

[16] H. Fei, Y. Yang, Z. Peng, G. Ruan, Q. Zhong, L. Li, E. L. G. Samuel, J. M. Tour, *ACS Appl. Mater. Interfaces* **2015**, *7*, 8083.

[17] S. Gao, G. D. Li, Y. Liu, H. Chen, L. L. Feng, Y. Wang, M. Yang, D. Wang, S. Wang, X. Zou, *Nanoscale* **2015**, *7*, 2306.

[18] J. Wang, D. Gao, G. Wang, S. Miao, H. Wu, J. Li, X. Bao, *J. Mater. Chem. A* **2014**, *2*, 20067.

[19] J. Deng, D. Deng, X. Bao, *Adv. Mater.* **2017**, *29*, 1606967.

[20] Y. Yang, Z. Lun, G. Xia, F. Zheng, M. He, Q. Chen, *Energy Environ. Sci.* **2015**, *8*, 3563.

[21] J. Deng, P. Ren, D. Deng, L. Yu, F. Yang, X. Bao, *Energy Environ. Sci.* **2014**, *7*, 1919.

[22] D. Deng, L. Yu, X. Chen, G. Wang, L. Jin, X. Pan, J. Deng, G. Sun, X. Bao, *Angew. Chem., Int. Ed.* **2013**, *52*, 371.

[23] Y. Yao, F. Chen, A. Nie, S. D. Lacey, R. J. Jacob, S. Xu, Z. Huang, K. Fu, J. Dai, L. Salamanca-Riba, M. R. Zachariah, R. Shahbazian-Yassar, L. Hu, *ACS Cent. Sci.* **2017**, *3*, 294.

[24] Y. Chen, Y. Li, Y. Wang, K. Fu, V. A. Danner, J. Dai, S. D. Lacey, Y. Yao, L. Hu, *Nano Lett.* **2016**, *16*, 5553.

[25] I. V. Thorat, D. E. Stephenson, N. A. Zacharias, K. Zaghib, J. N. Harb, D. R. Wheeler, *J. Power Sources* **2009**, *188*, 592.

[26] Y. Li, Y. Chen, A. Nie, A. Lu, R. J. Jacob, T. Gao, J. Song, J. Dai, J. Wan, G. Pastel, M. R. Zachariah, R. S. Yassar, L. Hu, *Adv. Energy Mater.* **2017**, *7*, 1601783.

[27] X. Cui, P. Ren, D. Deng, J. Deng, X. Bao, *Energy Environ. Sci.* **2016**, *9*, 123.

[28] C. Cui, L. Gan, M. Heggen, S. Rudi, P. Strasser, *Nat. Mater.* **2013**, *12*, 765.

[29] C. Cui, L. Gan, H.-H. Li, S.-H. Yu, M. Heggen, P. Strasser, *Nano Lett.* **2012**, *12*, 5885.

[30] Y. Li, K. K. Fu, C. Chen, W. Luo, T. Gao, S. Xu, J. Dai, G. Pastel, Y. Wang, B. Liu, J. Song, Y. Chen, C. Yang, L. Hu, *ACS Nano* **2017**, *11*, 4801.

[31] H. Wang, T. Maiyalagan, X. Wang, *ACS Catal.* **2012**, *2*, 781.

[32] Y. Shen, Y. Zhou, D. Wang, X. Wu, J. Li, J. Xi, *Adv. Energy Mater.* **2018**, *8*, 1701759.

[33] S. Wu, X. Shen, G. Zhu, H. Zhou, Z. Ji, L. Ma, K. Xu, J. Yang, A. Yuan, *Carbon* **2017**, *116*, 68.

[34] H. Zhang, Z. Ma, J. Duan, H. Liu, G. Liu, T. Wang, K. Chang, M. Li, L. Shi, X. Meng, K. Wu, J. Ye, *ACS Nano* **2016**, *10*, 684.

[35] J. K. Nørskov, T. Bligaard, A. Logadottir, J. R. Kitchin, J. G. Chen, S. Pandelov, U. Stimming, *J. Electrochem. Soc.* **2005**, *152*, 23.

[36] D. Voiry, H. Yamaguchi, J. Li, R. Silva, D. C. B. Alves, T. Fujita, M. Chen, T. Asefa, V. B. Shenoy, G. Eda, M. Chhowalla, *Nat. Mater.* **2013**, *12*, 850.

[37] W. Zhou, J. Zhou, Y. Zhou, J. Lu, K. Zhou, L. Yang, Z. Tang, L. Li, S. Chen, *Chem. Mater.* **2015**, *27*, 2026.

[38] M. Tavakkoli, T. Kallio, O. Reynaud, A. G. Nasibulin, C. Johans, J. Sainio, H. Jiang, E. I. Kauppinen, K. Laasonen, *Angew. Chem., Int. Ed.* **2015**, *54*, 4535.

[39] D. Merki, H. Vrubel, L. Rovelli, S. Fierro, X. Hu, *Chem. Sci.* **2012**, *3*, 2515.

[40] J. Zhang, T. Wang, P. Liu, S. Liu, R. Dong, X. Zhuang, M. Chen, X. Feng, *Energy Environ. Sci.* **2016**, *9*, 2789.

1801289 (8 of 8)